

# Gaussian ellipsoid model for confined polymer systems

Frank Eurich<sup>1</sup>, Philipp Maass<sup>1,2</sup> and Jörg Baschnagel<sup>3</sup>

<sup>1</sup>*Fachbereich Physik, Universität Konstanz, 78457 Konstanz, Germany*

<sup>2</sup>*Institut für Physik, Technische Universität Ilmenau, 98684 Ilmenau, Germany*

<sup>3</sup>*Institut Charles Sadron, 6 rue Boussingault, 67083 Strasbourg Cedex, France*

(February 22, 2002)

Polymer systems in slab geometries are studied on the basis of the recently presented Gaussian Ellipsoid Model [J. Chem. Phys. **114**, 7655 (2001)]. The potential of the confining walls has an exponential shape. For homogeneous systems in thermodynamic equilibrium we discuss density, orientation and deformation profiles of the polymers close to the walls. For strongly segregated mixtures of polymer components  $A$  and  $B$  equilibrium profiles are studied near a planar interface separating  $A$  and  $B$  rich regions. Spinodal decomposition processes of the mixtures in the presence of neutral walls show upon strong confinement an increase of the lateral size of  $A$  and  $B$  rich domains and a slowing down of the demixing kinetics. These findings are in agreement with predictions from time dependent Ginzburg–Landau theory. In the case, where one wall periodically favors one of the two mixture components over the other, different equilibrium structures emerge and lead to different kinetic pathways of spinodal decomposition processes in such systems.

## I. INTRODUCTION

The tailoring of polymer blends in thin film geometry is a problem of active current research<sup>1</sup> with a wide spectrum of possible technological applications. Of particular interest is the design of suitably patterned structures. Spontaneous phase separation processes of incompatible polymer blends may be used to translate a chemical pattern on the surface (as e.g. produced by the micro-contact printing technique) into a pattern of varying polymer compositions.<sup>2</sup> Another technique developed recently involves the alignment of polymer melts in inhomogeneous strong electric fields.<sup>3–5</sup>

Optimization of these processes requires knowledge of the long-time kinetics of polymeric systems on surfaces. Unfortunately, direct numerical investigation of this problem by means of molecular dynamics simulations is extremely difficult due to the enormous difference between typical vibrational times ( $\sim 1$  ps) and the characteristic time scales for diffusional processes of the macromolecules (of the order of seconds). One possible way to tackle this problem is to use dynamic self-consistent field theory,<sup>6</sup> which leads to coupled partial differential equations for the monomer densities of the various polymer components. Another promising approach was suggested based on the idea that on semi-macroscopic time and length scales, polymers can be regarded as soft particles with an ellipsoidal shape<sup>7</sup> (a different version of this idea, using soft spheres instead of ellipsoids, has recently been proposed<sup>8,9</sup>). In the work of Ref. 7, a bead spring model with repulsive Lennard-Jones interactions was used to determine the interaction parameters of the soft ellipsoids. Recently, we have set up a similar ellipsoidal model, where the parameters are derived from the Gaussian chain model instead.<sup>10</sup> While the underlying bead spring model is a more realistic basis for describing polymers, the Gaussian ellipsoid model (GEM) allows one to deal with effective interaction parameters

that are independent of the chain length, provided the self-interaction of the ellipsoids is taken into account.

In our previous work we have focused on bulk properties of polymer melts and mixtures, and verified that the model can faithfully reproduce the basic scaling relations and kinetic properties of polymeric systems on large time and length scales. In this publication we extend this study to systems in confined geometries. The interactions of the ellipsoids with the confining walls are modeled by a linear coupling of the monomer densities with an external wall potential. The latter is assumed to have an exponential form with decay length  $l_w$ , which is numerically very convenient and allows us to tune the softness of the wall by changing  $l_w$ . The detailed procedure to account for the wall interactions is presented in Sec. II. Some representative results for homopolymer systems are given in Sec. III. In particular, we show density profiles as well as wall induced shape and orientation effects. The main focus of this work is, however, to study phase separation phenomena in binary mixtures of two polymers  $A$  and  $B$ . In Sec. IV we provide evidence for surface directed spinodal decomposition waves, when the wall prefers one of the components  $A$  or  $B$ . In the case of neutral walls, lateral structure formation is observed in accordance with results derived on the basis of Ginzburg–Landau type treatments. Moreover, we quantify the orientation of the ellipsoids along the phase boundaries.

Finally, in Sec. V we consider structured systems, where one wall is considered to be chemically patterned and the magnitude  $\epsilon_w$  of the wall potential varies along one wall direction in a sinusoidal way with periodicity  $L_{\parallel}$ . This structuring of the surface induces a periodicity in the polymer melt. For large film thicknesses periodic polymer structures only occur in the vicinity of the patterned wall. When the film thickness becomes comparable to  $L_{\parallel}$ , the wall induced domain structure propagates through the film.

## II. WALL INTERACTIONS WITHIN THE GAUSSIAN ELLIPSOID MODEL

The Gaussian Ellipsoid Model is described in detail in a previous publication.<sup>10</sup> Therefore, we keep the definition of the model short and mainly present the necessary extensions to describe the interaction of the soft particles with the walls.

### A. Free Energy Functional

The free energy functional of an ensemble of  $M$  soft particles, corresponding to polymers with  $N$  bonds, is given by an intramolecular part, which accounts for the possible internal configurations, and an intermolecular part, which describes the interaction between the ellipsoids. In the presence of boundaries we add a term which accounts for the interaction between the particles and the surfaces,

$$F = F_{\text{intra}} + F_{\text{inter}} + F_{\text{wall}}. \quad (1)$$

The intramolecular part is determined by the probability  $P(\mathbf{S})$  for a polymer to have the eigenvalues  $\mathbf{S}$  of the radius of gyration tensor  $S_{\alpha\beta}$  (in order  $S_x \geq S_y \geq S_z$ ),

$$F_{\text{intra}} = \sum_{i=1}^M F_{\text{intra}}^{(i)} = -k_B T \sum_{i=1}^M \ln P(\mathbf{S}_i), \quad (2)$$

where  $k_B$  is the Boltzmann constant and  $T$  is the temperature. The intermolecular part is given by

$$F_{\text{inter}} = \frac{1}{2} \sum_{i=1}^M \sum_{j \neq i} F_{\text{inter}}^{(ij)} + \frac{1}{2} \sum_{i=1}^M F_{\text{inter}}^{(ii)}, \quad (3)$$

$$F_{\text{inter}}^{(ij)} = \hat{\epsilon} b^3 \int d^3 y \varrho'_i(\mathbf{y}) \varrho'_j(\mathbf{y}). \quad (4)$$

where the second term of eq. (3) accounts for the self-interaction of an ellipsoid. Equation (4) shows that the interaction energy is expressed in terms of the monomer densities of ellipsoids  $i$  and  $j$  (denoted by  $\varrho'_i(\mathbf{y})$  and  $\varrho'_j(\mathbf{y})$  in the laboratory system<sup>11</sup>). High monomer concentrations due to a contraction of a single ellipsoid (self-avoidance) or due to a strong overlap of two ellipsoids are disfavored energetically (mutual avoidance). The parameters  $\hat{\epsilon}$  and  $b^3$  are a ‘‘contact energy’’ and a ‘‘contact volume’’, respectively. We denote all reduced energy parameters without a hat, e.g.  $\epsilon = \hat{\epsilon}/k_B T$ . The parameter  $b$  sets the length scale of the model, i.e.  $b = 1$ .

The additional interaction term between the polymers and the walls is chosen to be of the form

$$F_{\text{wall}} = \sum_{i=1}^M F_{\text{wall}}^{(i)} = \sum_{i=1}^M \int d^3 y \varrho'_i(\mathbf{y}) V(z), \quad (5)$$

$$V(z) = \hat{\epsilon}_w \left[ \exp\left(-\frac{z}{2l_w}\right) + \exp\left(-\frac{L_z - z}{2l_w}\right) \right], \quad (6)$$

where  $\hat{\epsilon}_w$  is the strength of the monomer–wall interaction and the wall interaction range  $l_w$  characterizes the hardness of the wall. The slab thickness is given by  $L_z$ . Note, however, that for the special form of the external potential defined in eq. (6) two parameters  $\hat{\epsilon}_w/k_B T = 1$  and  $L_z$  are equivalent to two other parameters  $\hat{\epsilon}_w/k_B T = \epsilon_w$  and  $L_z - 2l_w \ln \epsilon_w$ , respectively, assuming all other parameters to be constant. Without loss of generality we therefore set  $\hat{\epsilon}_w/k_B T = 1$  in the following and define  $L_z$  as our film thickness. This is reasonable, since for  $l_w \rightarrow 0$  the system becomes confined by hard walls at positions  $z = 0$  and  $z = L_z$ .

An exponential wall potential is frequently used to model a laterally structureless and purely repulsive wall.<sup>12</sup> Here, it has the advantage, that the overlap between the potential and the monomer densities, that are of Gaussian form, are analytically integrable. The formulas are given in appendix A. By choosing small values for  $l_w$  one can model hard substrates, while for large  $l_w$  one models soft substrates, that e.g. correspond to polymer films on polymer brushes.<sup>13</sup> We note that the unperturbed monomer densities are used in eq. (5). Hence, we do not a priori build in layering effects which are typically observed in simulations of polymer melts close to walls.<sup>14</sup> This is in the spirit of the GEM, where the unperturbed chain is used as input and all other properties are determined by interaction terms. In summary, eqs. (1–6) define the thermodynamics of the model for a homogeneous system of ellipsoids in a film geometry.

To generalize the model to binary mixtures of ellipsoids of type  $A$  and  $B$  in films, we choose an equal interaction between polymers of the same type  $\hat{\epsilon}_{AA} = \hat{\epsilon}_{BB} = \hat{\epsilon}$ , while the interaction between unlike polymers is enhanced by a mismatch  $\delta$ , i.e.  $\hat{\epsilon}_{AB} = \hat{\epsilon}(1 + \delta)$ . The same degree of polymerization, i.e.  $N_A = N_B = N$ , is assumed for both components. To account for different interactions between the substrates and the two components, we introduce an additional wall mismatch parameter  $\delta_w$ , with  $-1 < \delta_w < 1$ . The interaction parameters  $\hat{\epsilon}_w(1 + \delta_w)$  and  $\hat{\epsilon}_w(1 - \delta_w)$  refer to the  $A$ - and  $B$ -components, respectively. Note that the mismatch parameters  $\delta$  and  $\delta_w$  only change the strength of the repulsive monomer–monomer or monomer–wall interactions. Phase separation is thus driven by the disparity of excluded volume interactions, and not by attraction.

The kinetic properties of the GEM are given by a discrete time Monte-Carlo algorithm, where three different moves of the ellipsoids are allowed: Translation of the center of mass, free rotation of the principal axis and deformation, i.e. a change of the eigenvalues  $\mathbf{S}_i$ . For details we refer the reader to Ref. 10.

## B. Parameters and Geometry in Film Simulations

The simulations in this work were carried out for ellipsoids corresponding to a chain length of  $N = 50$ . The number of particles is  $M = 2000$  in the case of homogeneous systems and  $M = 4000$  for binary mixtures. We always choose  $\epsilon_w = \epsilon = 1$ .

For binary mixtures a symmetric composition is considered, where the fraction of the  $A$ -component is  $f_A = 0.5$ . For given film thickness  $L_z$  we determine the lateral dimension  $L$  by requiring a constant “bulk monomer concentration”  $c = M(N+1)/L_z L^2 = 0.85$ . Tables I and II list the geometries of the simulated systems.

The homogeneous systems are thermalized several thousand Monte Carlo steps (MCS) and averaged over at least 10000 MCS. In the case of binary mixtures, the phase diagrams were determined in the semi-grand canonical ensemble. Averages are performed over several thousand MCS.

## III. EFFECTS OF HARD WALLS ON HOMOGENEOUS SYSTEMS

In this section we present the results for homogeneous ellipsoid systems bound by two walls. As the focus of this work will be on binary mixtures in confined geometries, we defer a more detailed analysis of homogeneous systems in a slab to a forthcoming publication.

As a reference length to compare with, we use the unperturbed average radius of gyration in a bulk system with monomer concentration  $\bar{c} = 0.85$ , which is given by, cf. Ref. 10,

$$\bar{R}_G = 3.6. \quad (7)$$

### A. Concentration of Monomers and of Centers of Mass

The results for the concentration of the monomers

$$c(z) = \sum_{i=1}^M \int dx dy \varrho'_i(\mathbf{y}) \quad (8)$$

and the concentration of the centers of mass  $c_{\text{cm}}$  are shown in Fig. 1 for a thick film ( $L_z = 25$ ), where bulk-like features are found inside the slab. Two wall interaction ranges are considered. In the first case,  $l_w = 0.5$ , meaning that  $2l_w$  is equal to the average bond length of the Gaussian chain molecules, while in the second case the interaction range is much smaller,  $l_w = 0.15$ , modeling a harder wall. In both cases, the concentration profiles rapidly decay to zero as  $z \rightarrow 0$ . However, whereas the profile of the center of mass,  $c_{\text{cm}}$ , is zero at  $z = 0$ , justifying our definition of the film thickness, the monomer concentration vanishes only for  $z < 0$ . This behavior

reflects the softness of the wall potential, which is also responsible for less pronounced layering effects, typically observed in polymer melts confined between strongly repulsive walls.<sup>14,15</sup> Here, we find the signature of these density oscillations only for  $l_w = 0.15$ , whereas the softer wall gives rise to a monomer profile comparable to that obtained for small bulk concentrations in the hard wall case.<sup>16,17</sup>

The monomer concentration profiles for different film thicknesses  $L_z$  are shown in Fig. 2 for the case  $l_w = 0.5$ . For the thicker slabs ( $L_z = 17, 25$ ) a plateau in the profiles is reached at a distance of about  $2\bar{R}_G$  from the wall. However, the plateau value still varies slightly with the system size and is larger than the bulk value  $\bar{c} = 0.85$ , that will be obtained for  $L_z \rightarrow \infty$ . For  $L_z < 4\bar{R}_G$  the films do not show bulk-like behavior any more. The profile rather runs through a pronounced maximum  $c_{\text{max}}$  at  $z = L_z/2$ .

If  $L_z$  decreases, starting from  $L_z = 25$ ,  $c_{\text{max}}$  first increases, since the reduction of the monomer density close the walls becomes more relevant for the overall film behavior, the smaller the thickness is. It has to be compensated by a higher density in the film center to keep the density constant. For  $L_z < 4$ , however, we observe the opposite trend, i.e. a decrease of  $c_{\text{max}}$ . This is due to the fact that the overlap of the wall potentials becomes important. This overlap effectively decreases the gradient of the wall potential and thus allows the monomers to penetrate the wall more deeply. The increased monomer density in the wall region entails a reduction of the density in the middle of the film in comparison to the thicker films. The relative changes of  $c_{\text{max}}$  are about 20 percent. In the case of harder walls ( $l_w = 0.15$ ) we found a stronger variation and a largest value  $c_{\text{max}} = 1.36$  is obtained for  $L = 3$ . With respect to the binary mixtures studied in Sec. IV we wanted to keep the influence of these concentration variations small. We thus chose  $l_w = 0.5$  in the following. However, very similar results could have been obtained for  $l_w = 0.15$ .

### B. Orientation

In this section we study the orientation of the ellipsoids as a function of the distance of the center of mass,  $z$ , from the wall.

Let us denote by  $\mathcal{R}_{\alpha\beta}$  the matrix, that defines the orientation of the principal axis with respect to the laboratory coordinate system. As  $\mathcal{R}_{\alpha\beta}$  consists of the normalized eigenvectors of the principal axis system,  $\sum_{\beta} \mathcal{R}_{\alpha\beta}^2 = 1$  holds. In an ensemble of randomly oriented ellipsoids the average value of all squared matrix elements is  $\langle \mathcal{R}_{\alpha\beta}^2 \rangle = 1/3$ . Thus we expect this value for large distances  $z$  from the walls. A parallel orientation of one of the principal axis  $\alpha$  to the laboratory axis  $\beta$  corresponds to  $\langle \mathcal{R}_{\alpha\beta}^2 \rangle = 1$ , while a perpendicular orientation corresponds to  $\langle \mathcal{R}_{\alpha\beta}^2 \rangle = 0$ . Hence  $\mathcal{R}_{\alpha\beta}^2$  is a convenient

measure to characterize the orientation. In the following, we denote an average of some quantity  $Q$  over all particles, whose center of mass is at distance  $z$  from the left wall by  $\langle Q(z) \rangle$ .

Figure 3 shows the results for the orientation of the principal axis with respect to the  $z$ -axis, i.e. perpendicular to the walls for different film thicknesses. We remind the reader that the system of principal axes is chosen such that  $S_x \geq S_y \geq S_z$ . For thick films ( $L_z = 17$ ), we find  $\langle \mathcal{R}_{\alpha z}^2(z) \rangle = 1/3$  far from the walls, as expected. When approaching the wall the smallest principal axis,  $z$ , becomes aligned perpendicular to the wall,  $\langle \mathcal{R}_{zz}^2(z) \rangle \approx 1$ , while the other two principal axes become aligned parallel.<sup>18</sup> This behavior is observed for all film thicknesses and is also found in other simulations.<sup>19</sup>

The anisotropy in the orientation occurs on a length scale  $2\bar{R}_G$  at most. The range is smaller along the  $y$ -principal axis than along the  $x$ -principal axis, since due to  $S_x > S_y$  the energy cost for a rotation of the  $y$ -axis in the direction of the  $z$ -laboratory axis is smaller than that of the  $x$ -principal axis. It is remarkable that the anisotropy effect shows only very little dependence on the film thickness, even when  $L_z$  becomes comparable to or smaller than  $\bar{R}_G$ .

### C. Deformation

Figure 4 shows how the shape of the ellipsoids is altered by the presence of the walls. For large distances, we find that the averaged eigenvalues  $\langle S_\alpha(z) \rangle$  are independent of  $z$  and coincide with the bulk values. These values, determined from the data of Ref. 10, are  $\bar{S}_x = 10.1$ ,  $\bar{S}_y = 2.0$  and  $\bar{S}_z = 0.71$ .

However, the ellipsoids near the walls are distorted. The size of the two major axes  $x$  and  $y$  is enhanced, whereas  $\langle S_z(z) \rangle$  is reduced. When  $z$  increases,  $\langle S_z(z) \rangle$  approaches the bulk value almost monotonously, while  $\langle S_x(z) \rangle$  and  $\langle S_y(z) \rangle$  run through a minimum before crossing over to the bulk behavior.<sup>18</sup> This means that the ellipsoids near the surface are strongly oblate. This influence of a repulsive wall on the structure of the chains is also confirmed by other simulations (see Ref. 15,19 and references therein). As the film thickness  $L_z$  decreases, we find that the maximal values of  $\langle S_z(z) \rangle$  become smaller for  $L_z < 2\bar{R}_G$ .

### D. Discussion

Combining the results of the orientational properties and the deformation we find that ellipsoids at a distance  $z > 2\bar{R}_G$  are virtually unperturbed by the boundaries and exhibit bulk behavior. On approaching the walls there is a slight deformation of the two major principal axes, accompanied by an alignment of the principal axes. This alignment continues monotonously, up to the point,

where the smallest principal axis of the ellipsoids is oriented perpendicular to the walls. Near the walls, the ellipsoids are compressed in  $z$ -direction and elongated with respect to the two major axes, thus exhibiting an almost two-dimensional behavior.

It is interesting to compare these findings with results obtained by other authors. Let us mention that the analysis of the shape of polymers near walls is usually based on ‘‘components’’ of the radius of gyration with respect to the laboratory system. These components are the square roots of the diagonal elements of the radius of gyration tensor,

$$R_{G\alpha} = \sqrt{S_{\alpha\alpha}} \text{ or } R_{G\parallel}^2 \equiv S_{xx} + S_{yy}, R_{G\perp}^2 \equiv S_{zz}. \quad (9)$$

It is clear that

$$S_{\alpha\beta} = \sum_{\gamma} \mathcal{R}_{\gamma\alpha} S_{\gamma} \mathcal{R}_{\gamma\beta}, \text{ esp. } S_{\alpha\alpha} = \sum_{\gamma} \mathcal{R}_{\gamma\alpha}^2 S_{\gamma}. \quad (10)$$

This kind of analysis makes it difficult to distinguish between an orientation and a deformation of the polymer coils.

When calculating the quantities  $\langle R_{G\parallel}^2(z) \rangle$  and  $\langle R_{G\perp}^2(z) \rangle$  for our model, we find reasonable agreement with the results of other simulations (see Ref. 15,19 and references therein), namely an increase of  $\langle R_{G\parallel}^2(z) \rangle$  near the wall and a strong decrease of  $\langle R_{G\perp}^2(z) \rangle$ . The results for  $\langle R_{G\parallel}^2(z) \rangle$  are similar to that for  $\langle S_x(z) \rangle$  and  $\langle S_y(z) \rangle$  in Fig. 4, and the results for  $\langle R_{G\perp}^2(z) \rangle$  are similar to  $\langle S_z(z) \rangle$ , except that the extrema near the walls are more pronounced.

Pai–Panandiker et. al.<sup>20</sup> examined orientational effects of the end-to-end vector in a Monte-Carlo Simulation of dense polymer films. They found an increasing alignment of the end-to-end vector with reducing  $L_z$ , but averaged their quantities over the whole film. As there is a strong correlation between the end-to-end vector and the major principal axis  $x$ , their results support the picture presented above.

The work of Vliet and Brinke<sup>21</sup> is dealing with a principal axis transformation to analyze orientational degrees of freedom, for a single self-avoiding walk confined between two hard walls. The main conclusion of this work is that with decreasing film thickness the principal axis of the polymers are aligned due to the confinement, long before their shape changes. While their situation is not directly comparable to the case of a polymer melt between two plates considered here, our results support the view that the orientational effect is dominant. This is not unexpected, as a reorientation of the polymer only constraints on one or two degrees of freedom, while a deformation affects the whole chain statistics, therefore affecting of the order of  $N$  degrees of freedom.

#### IV. DEMIXING PROCESSES IN THIN FILMS

In this section we consider the effect of two neutral ( $\delta_w = 0$ ) and planar walls on a binary mixture of ellipsoids. Results will be discussed for fixed  $l_w = 1/2$ .

##### A. Dependence of Phase Diagram on Film Thickness

For temperatures below a critical temperature  $T_c$ , separation into two phases, rich in type  $A$  and type  $B$  polymers, occurs. First, we determine how  $T_c$  depends on film thickness  $L_z$ . Ginzburg–Landau theory<sup>22</sup> predicts and simulations<sup>23</sup> have shown that

$$\frac{T_c(\infty) - T_c(L_z)}{T_c(\infty)} \propto \frac{1}{L_z}, \quad L_z \ll Nb, \quad (11)$$

$$\frac{T_c(\infty) - T_c(L_z)}{T_c(\infty)} \propto \frac{1}{L_z^2}, \quad L_z \gg Nb. \quad (12)$$

Equations (11,12) hold as long as the chain conformations are virtually unperturbed, i.e.  $L_z > \bar{R}_G$ , and mean field theory applies. This requires that the bulk correlation length  $\xi$  (characterizing the interfacial width close to  $T_c$ ) is smaller than the crossover length<sup>23</sup>  $\xi_\times \propto Nb$ , which determines the change from Ising–type to mean field behavior. While for  $L_z \ll Nb$  the surface interaction is dominant [eq. (11)], it is the finite size of the film, which determines the shift of  $T_c$  for  $L_z \gg Nb$  [eq. (12)]. Since  $N = 50$  and  $2 \leq L_z \leq 25$  in our case, we expect eq. (11) to apply, at least for  $L_z > \bar{R}_G = 3.6$  [eq. (7)].

For the sake of efficiency the simulations are carried out in a semi–grand canonical ensemble,<sup>24</sup> i.e. the total number of particles is fixed, while the fractions  $f_A$  and  $f_B$  of  $A$  and  $B$  polymers can fluctuate. Figure 5 shows the order parameter  $\langle |f_A - f_B| \rangle$  as a function of the mismatch parameter  $\delta$  for various  $L_z$ .

In order to test the expectation that our model obeys eq. (11), we simply estimated  $\delta_c \propto 1/T_c$  from an extrapolation of the steepest descent of the coexistence curve to zero. No detailed finite size analysis of the lateral dimension  $L$  was attempted. Such an analysis does not seem to be really necessary, since  $T_c(L, L_z)$  monotonously approaches the asymptotic limit  $T_c(L_z)$  for large enough  $L$ .<sup>23</sup> For the  $L$ -values used in this study (see Table II), inspection of Fig. 5 of Ref. 23 suggests that qualitatively reliable results should be obtained from our estimates of  $T_c$ . In fact, we see that  $T_c$  decreases with  $L_z$ . The inset of Fig. 5 shows that  $T_c(L_z) - T_c(\infty) \propto -1/L_z$ , in agreement with eq. (11).

##### B. Orientation at Phase Boundaries

To study the influence of phase boundaries on the internal degrees of freedom of the ellipsoids, we prepared a fully phase separated system with periodic boundary conditions in all directions  $L = L_z = 62.14$ . The  $A$ -ellipsoids

are randomly distributed in the half–space  $z = (0, L_z/2)$  and the  $B$ -ellipsoids in the half–space  $z = (L_z/2, L_z)$ . We chose  $\delta = 0.2$ , which corresponds to the strong segregation regime (cf. Fig. 5) for thick films. The system was thermalized for 2000 MCS, a time much larger than the autocorrelation time of the internal degrees of freedom (shape and orientation). Moreover, this time is sufficient for an ellipsoid to diffuse typically over the distance from one interface to the center of one of the two phases. All averages were recorded over additional 18000 MCS.

In Fig. 6a the different center of mass densities for both components  $c_{\text{cm},A}$ ,  $c_{\text{cm},B}$ , and  $c_{\text{cm}} = c_{\text{cm},A} + c_{\text{cm},B}$ , normalized by the chain length ( $N = 50$ ) are displayed. We see that the total density  $c_{\text{cm}}$  of the ellipsoids becomes smaller at the interfaces in order to reduce the interaction between the mixture components. An additional effect occurs in Fig. 6b, where the squared matrix elements  $\langle \mathcal{R}_{\alpha z}^2 \rangle$  are shown. Comparable to the behavior near a wall (cf. Sec. III B) the ellipsoids align their  $x$ -axis (largest principal axis) parallel to the interface, while the  $z$ -axis (smallest principal axis) tends to be oriented perpendicular to the interface. However, this effect is much less pronounced than for walls. In particular, there is almost no effect on the orientation of the  $y$ -axis.

Finally, Fig. 6c characterizes the deformation of the ellipsoids via the eigenvalues  $S_\alpha$  that are normalized by their bulk values. Near the interfaces the ellipsoids are compressed with respect to all axes. The relative compression increases with the length of the principal axis, meaning that the asphericity becomes reduced. This effect was also observed in extensive Monte Carlo simulations of the bond-fluctuation lattice model<sup>25</sup> and is analogous to the reduction of the radius of gyration in a strongly segregated mixture, where the polymers of the minority component shrink to reduce energetically unfavorable contacts with the surrounding majority phase.<sup>10,26</sup>

##### C. Spinodal Decomposition Between Neutral Walls

Studies based on time–dependent Ginzburg–Landau theory<sup>27</sup> have shown that for spinodal decomposition in thin neutral films lateral decomposition waves of a characteristic wavelength  $k_{\parallel,m}$  characterize the domain pattern at short times, where the concentration inside the  $A$  and  $B$  rich domains has not yet reached the equilibrium value. These studies predict that  $k_{\parallel,m}$  becomes smaller with decreasing  $L_z$ , when  $L_z \lesssim \lambda_m$ , where  $\lambda_m$  denotes the bulk demixing length. Furthermore, if  $L_z \lesssim \lambda_m$ , the growth rates of the decomposition modes become smaller so that the overall demixing process slows down. These predictions will be tested here for the GEM.

We consider a system confined between two planar and neutral walls ( $\delta_w = 0$ ) that is prepared at infinite temperature at a time  $t < 0$ . All orientations and particle

positions are random and the distribution of the eigenvalues is given by those of free Gaussian chains. At  $t = 0$  we quench the system into the spinodal region of the phase diagram by setting  $\epsilon \equiv \hat{\epsilon}/k_B T = 1$  and  $\delta = 0.2$  (for  $L_z = 2$  we used  $\delta = 0.25$ ). The dynamics of the system is specified by Monte-Carlo moves of the individual ellipsoids corresponding to translations, reorientations and deformations. The detailed procedure is described in Ref. 10.

To quantify the demixing process of the films, we determine the lateral intermediate scattering function

$$I_{\parallel}(k_{\parallel}, z, t) = \langle \rho_{A\parallel}(\mathbf{k}_{\parallel}, z, t) \rho_{A\parallel}(-\mathbf{k}_{\parallel}, z, t) \rangle - c_A^2 \delta(k_{\parallel}), \quad (13)$$

where  $\rho_{A\parallel}(\mathbf{k}_{\parallel}, z, t)$  is the Fourier transform of the total monomer density  $\varrho'_A(\mathbf{y}, t) = \sum_{i=1}^{M_A} \varrho'_{i,A}(\mathbf{y}, t)$  of the  $A$ -chains with respect to the lateral coordinates  $x, y$ . The power-spectrum depends on  $k_{\parallel} \equiv (k_x^2 + k_y^2)^{1/2}$  only, therefore it is possible to perform an additional circular average<sup>28</sup> in the  $k_x, k_y$ -space. An explicit expression for  $\rho_{A\parallel}(\mathbf{k}_{\parallel}, z, t)$  is given in appendix B.

Figures 7a-c show  $I_{\parallel}(k_{\parallel}, z, t)$  for a slab of thickness  $L_z = 6$  and various fixed times. As one can see from these figures,  $I_{\parallel}(k_{\parallel}, z, t)$  exhibits a maximum that corresponds to a characteristic size  $2\pi/k_{\parallel,m}$  of the  $A$  and  $B$  rich domains in the lateral direction. With increasing time the maximum grows and shifts to smaller values of  $k_{\parallel}$ , reflecting lateral domain coarsening.

To quantify the speed of this domain coarsening and to examine its dependence on film thickness  $L_z$ , we consider the first moment of  $I_{\parallel}(k_{\parallel}, z, t)$  averaged over  $z$ ,<sup>10</sup>

$$k_{1,\parallel}(t) \equiv \frac{1}{L_z} \int_0^{L_z} dz \frac{\int_0^{\infty} dk_{\parallel} k_{\parallel} I_{\parallel}(k_{\parallel}, z, t)}{\int_0^{\infty} dk_{\parallel} I_{\parallel}(k_{\parallel}, z, t)}. \quad (14)$$

This quantity is a measure of the average lateral domain size as a function of time. The results are given in Fig. 8 for different values of  $L_z$ .

In our system the bulk demixing length  $\lambda_m$  can be estimated by  $\lambda_m \approx 2\pi/k_1(t_0) \approx 14$ , cf. Fig. 15 of Ref. 10 ( $t_0 = 500$  MCS). From this we expect that the effects predicted by time-dependent Ginzburg-Landau theory should occur for  $L_z \lesssim 14$ .

Indeed, we find that  $k_{1,\parallel}(t_0)$  determined at  $t_0 = 1000$  MCS shrinks with decreasing  $L_z$ , cf. Fig. 8. Moreover, in the thinner films the coarsening sets in later, which is illustrated by the fact that curves at equal times have a steeper slope for thick films than for thin ones. This supports the result that the growth rates of the decomposition modes decrease. We note that these effects are not due to a shift of the critical temperature  $T_c$  with  $L_z$ . We carried out additional simulations with a mismatch  $\delta = 0.3$  for  $L_z = 2, 3, 4$  and found that the lateral demixing length depends only weakly on the mismatch parameter at fixed film width.

To summarize this section, our results support the predictions of Ref. 27, i.e. the increase of the lateral demixing

length and the slowing down of the demixing kinetics for  $L_z < \lambda_m$ . This qualitative agreement with the results of Ref. 27 is obtained without any special wall potential or tuning of the parameters, supporting the view that the effects occur quite generally. However, a suppression of spinodal decomposition below a critical film thickness  $L_c$ , as predicted in Ref. 27, is not found. This is due to the fact that noise terms in the kinetic equations of the theory have been neglected.

#### D. Surface Directed Spinodal Decomposition

In the case, where one wall preferentially attracts one of the two components, surface directed spinodal decomposition waves<sup>29</sup> (SDW) form when a homogeneous mixture is quenched into a thermodynamically unstable part of the phase diagram. However, in thin films the SDW might be “suppressed” by the confinement.<sup>30</sup>

Here, we investigate the case, where both walls attract ellipsoids of component  $B$ . Figure 9 shows the emerging monomer concentrations  $c_B(z)$ , averaged over the lateral dimensions. For rather large slabs ( $L_z = 50$ ) symmetric SDW’s form, cf. Fig. 9a. Their wavelength at short times is given by the bulk demixing length  $\lambda_m \approx 14$ , and at large times increases due to domain coarsening. Finally, at  $t = 100000$  MCS a  $B$ - $A$ - $B$  stripped pattern has formed in the  $z$ -direction. In the case of thin films ( $L_z = 12.5$ , cf. Fig. 9b), this kind of pattern emerges already for short times ( $t = 1000$  MCS). For  $L_z < \lambda_m$  the propagation of the SDW is suppressed, and only a fast segregation of the  $B$ -components at the walls occur. For even thinner films ( $L_z = 6$ ) the two maxima seen in Fig. 9b, are less pronounced and merge into one in the case of  $L_z = 3$ .

#### V. STRUCTURED SURFACES

In this section we study polymer mixtures between two walls where one of the two surfaces is chemically patterned. One part of the patterned wall attracts component  $A$ , while the other part attracts component  $B$ . The second homogeneous wall is neutral with respect to the two components. The surface pattern is a periodic arrangement of equally spaced stripes, cf. Fig. 10, modeled by a surface potential

$$V(z) = \hat{\epsilon}_w \exp\left(-\frac{z}{2l_w}\right) \left[1 \pm \delta_w \cos\left(\frac{2\pi y}{L_{\parallel}}\right)\right]. \quad (15)$$

The positive sign refers to component  $A$ , the negative to component  $B$ . As for homogeneous walls, the overlap integral [eq. (5)] can be calculated analytically, see App. A. In the following we consider the case  $l_w = 0.5$  and  $\delta_w = 0.5$ , where both components are strongly favored by the respective parts of the wall. Our focus will

be on the influence of the film thickness  $L_z$  and of the pattern periodicity  $L_{\parallel}$  on the demixing process.

### A. Structural Phase Diagram

From a technological point of view it is important to explore regions in  $L_z$ - $L_{\parallel}$  space, where the pattern of the surface can be translated into a corresponding polymer structure that pervades the whole film.<sup>2,31</sup>

We carried out simulations in a semi-grand canonical ensemble for different combinations of  $L_z$  and  $L_{\parallel}$  summarized in Tab. III. As we require  $L_y$  to be an integer multiple of  $L_{\parallel}$  and work with a fixed number of particles  $M = 4000$ , we adjusted  $L_x$  so that the monomer density (or volume) is constant. The quantities of interest are determined after an equilibrated stationary domain pattern has evolved.

To characterize the equilibrium patterns we recorded the center of mass density  $c_{\text{cm}}$ . Two representative results for a slab of thickness  $L_z = 6$  are given in Fig. 11. It shows the normalized center of mass density  $(N+1)c_{\text{cm}}$  as a function of one laboratory axis ( $y$  or  $z$ ), while the density profile was integrated over the respective remaining axes. For  $L_{\parallel} = 25$ , Fig. 11a, the  $A$  and  $B$  ellipsoids are separated in a periodic manner due to the structure of the wall. As one can see from the inset, this structure propagates through the whole film (“full structure”). By contrast, for  $L_{\parallel} = 6$ , Fig. 11b, the periodic behavior is confined to a small region near the structured surface (cf. the inset). In this case, small cylindrical caps of one phase are present at the favored parts of the surface (“partial structure”). These situations, full and partial structures, are schematically depicted in Fig. 10.

A systematic study of the emerging structures as a function of  $L_z$  and  $L_{\parallel}$  is shown in Fig. 12. The  $(L_{\parallel}, L_z)$ -plane is divided into two regions, where systems with small  $L_{\parallel}$  and large  $L_z$  are only partially structured, while systems with large  $L_{\parallel}$  and small  $L_z$  are fully structured. To explain this behavior, we associate with the half periods of the cosine term in eq. (15) two homogeneous surface regions  $\gamma$  and  $\delta$ , cf. Fig. 10. The contact angles in these regions are

$$\cos \Theta_{\gamma} = \frac{\sigma_{A\gamma} - \sigma_{B\gamma}}{\sigma_{AB}} \quad \cos \Theta_{\delta} = \frac{\sigma_{A\delta} - \sigma_{B\delta}}{\sigma_{AB}}. \quad (16)$$

Near the  $\gamma$ - $\delta$  interface the contact angle  $\Theta$  can assume any value between the two limiting cases  $\Theta_{\gamma}$  and  $\Theta_{\delta}$ .<sup>32</sup> Requiring without loss of generality that  $c_A \leq c_B$ , the contact angle is restricted to  $0 \leq \Theta \leq \pi/2$ . A simple consideration of the area of the interfaces in both cases (a) and (b) given in Fig. 10 yields a difference of the free energy

$$\Delta F = \sigma_{AB} L_x L_y \left( 2L_z - \frac{\Theta}{2 \sin \Theta} L_{\parallel} \right). \quad (17)$$

The transition between both structures occurs, if  $\Delta F = 0$ , resulting in

$$\frac{L_z}{L_{\parallel}} = \frac{\Theta}{4 \sin \Theta}. \quad (18)$$

The crossover regime between the two structures in the  $L_z$ - $L_{\parallel}$  diagram is between the two lines with slope  $1/4$  (for  $\Theta \rightarrow 0$ ) and slope  $\pi/8$  (for  $\Theta \rightarrow \pi/2$ ). Both lines are marked in Fig. 12 for comparison, showing agreement with the simulations.

This result is also confirmed by experiments of an  $A/C$  demixing process in thin films.<sup>31</sup> In the experiment, the patterned substrate was realized by physisorbing the  $B$ -component of an  $ABC$  triblock copolymer microphase separated brush. This leads to a checkerboard like  $A/C$  surface structure, instead of the striped structure considered above. However, the different geometry yields only a different constant in the righthand side of eq. (18).

### B. Pattern Directed Spinodal Decomposition

In this section we consider the kinetics of a system similar to the one described in the previous section, but for fixed fraction  $f_A = 0.5$ . The initial conditions are as in Sec. IV C.

The intermediate scattering function

$$I_y(k_y, z, t) = \int_0^{\infty} dk_x I_{\parallel}(\mathbf{k}_{\parallel}, z, t), \quad (19)$$

with  $I_{\parallel}(\mathbf{k}_{\parallel}, z, t)$  given in eq. (13) characterizes the domain formation with respect to the pattern-direction.

Figure 13 shows  $I_y(k_y, z, t)$  for a thin slab of thickness  $L_z = 6$  and pattern periodicity  $L_{\parallel} = 25$ , corresponding to a full structure in equilibrium, at two times. At early times ( $t = 1000$  MCS, see Fig. 13a), a dominant structure arises near the patterned substrate on the length scale  $k_y^{-1} = L_{\parallel}/2\pi$ . This structure propagates in  $z$ -direction until it reaches the opposite wall ( $t = 10000$  MCS, see Fig. 13b). At later times, this structure is stable, as one would expect from Fig. 12. We determined no further change in  $I_y(k_y, z, t)$  until  $t = 30000$  MCS.

Figure 14 shows  $I_y(k_y, z, t)$  for a film of thickness  $L_z = 25$  and pattern periodicity  $L_{\parallel} = 12.5$ , corresponding to a partial structure in equilibrium. In this system the pattern-induced demixing is much faster than the lateral spinodal decomposition. The pattern-induced structure for small values of  $z$  leads to a much larger corresponding peak in  $I_y(k_y, z, t)$ , Fig. 14a, than the disordered lateral domain pattern emerging for larger  $z$ . The ordered periodic structure propagates into the film over a finite distance only ( $z \approx 6$ , see Fig. 14b). For later times ( $t = 30000$  MCS), the amplitude of the lateral decomposition waves is comparable to the amplitude of the pattern-induced waves. However, the peak in  $I_y(k_y, z, t)$  occurs at smaller values of  $k_y$ . Thus, the periodic domain

structure is stable near the patterned wall, but further away the domain pattern coarsens.

Such a behavior, i.e. a rapid formation of a patterned equilibrium structure in thin films, but a lateral domain coarsening afterwards in thick films, has also been observed in numerical treatments of the Cahn–Hilliard equation with appropriate boundary conditions,<sup>33,34</sup> and in experiments.<sup>33</sup>

In both cases considered so far the periodicity  $L_{\parallel}$  was comparable to or larger than the bulk demixing length  $\lambda_m$ . The question arises of what happens for  $L_{\parallel} \ll \lambda_m$ . In this case, we expect that the patterned surface induces structures, which are too small to drive spinodal decomposition because the interfacial energy of such structures is higher than the free energy gained by decomposition.

To investigate the interplay between the two length scales  $L_{\parallel}$  and  $\lambda_m$  we consider a slab of thickness  $L_z = 12.5$  and vary  $L_{\parallel}$ .<sup>35</sup> Figure 15 shows corresponding lateral structure factors  $I_y(k_y, z, t)$  for  $t = 1000$  MCS and for  $L_{\parallel} = 6, 12.5$ , and  $25$ . In the case of  $L_{\parallel} = 6 \ll \lambda_m$ , Fig. 15a, the peaks corresponding to the surface induced structure and the lateral modes are comparable. The demixing process is not dominated by the surface-induced pattern. Also, the induced structure develops much more slowly compared to the case of  $L_{\parallel} = 12.5 \simeq \lambda_m$ , shown in Fig. 15b. In this case, the peak corresponding to the ordered structure is a factor of about 10 higher, and the lateral demixing modes are thus almost invisible. For  $L_{\parallel} = 25 \gg \lambda_m$  a double peak structure emerges. This can be interpreted in terms of a pattern directed spinodal decomposition wave, i.e. if one looked at the concentration fluctuations  $\delta c_A(\mathbf{y}) = \varrho'_A(\mathbf{y}) - c_A$  in the  $yz$ -plane and labeled positive and negative regions of  $\delta c_A(\mathbf{y})$  black and white respectively, one would see a checkerboard-like pattern.<sup>34</sup>

To see more directly how in the last case such a pattern propagates into the film, we plotted in Fig. 16 the intermediate scattering function  $I_y(2\pi/L_{\parallel}, z, t)$  as a function of  $z$  for various times  $t$  for a system with  $L_z = 25$  and  $L_{\parallel} = 50$ . This picture describes how the surface-induced periodic domain patterns grow in perpendicular direction. Since our film thickness is limited, we did not try to quantify the propagation of this kind of kinetics further. For very large film thicknesses we would expect the usual Lifshitz–Slyozov domain growth to occur at large times.

## VI. SUMMARY

The Gaussian Ellipsoid Model<sup>10</sup> (GEM) is based on the fact that the most probable shape of a polymer is not spherical, but ellipsoidal.<sup>36–38</sup> This ellipsoid resembles a flattened American football, the eigenvalues  $\mathbf{S}$  of the three principal axes being all different. In the GEM, the eigenvalues and their distribution are calculated for a Gaussian chain. Thus, the model should faithfully rep-

resent the large scale chain structure in a  $\Theta$ -solvent or in a melt. In order to extend the model to dilute and semi-dilute solutions in good solvents excluded volume interactions have to be added. This is achieved by determining the local monomer density in the Gaussian ellipsoid. A strong overlap of the density in the ellipsoid or between different ellipsoids entails a large energy penalty which mimics the self- and mutual excluded volume interaction of soft polymer coils.

In the bulk, the model reproduces well established properties on large length and time scales.<sup>10</sup> For homopolymers, it yields the correct crossover scaling from dilute to semi-dilute solutions and the correlation hole in the melt. For symmetric homopolymer mixtures, one (approximately) finds a linear dependence of the critical temperature on chain length, a contraction of the chain size of the minority component, and a Lifshitz–Slyozov behavior for the late stages of spinodal decomposition.

These results prompt us to test the model if interfaces are present. These interfaces are either self-generated, as it is the case in the strong-segregation regime of binary polymer mixtures, or imposed externally by the introduction of two repulsive walls on opposite sides of the simulation box. The main results of this extension may be summarized as follows:

(1) In the vicinity of a repulsive wall the ellipsoids can no longer adopt all possible orientations. They become aligned and distorted. The two longer axes are stretched and oriented parallel to the wall, whereas the short axis shrinks and orients perpendicular to it. These wall-induced perturbations of the chain’s structure cross over to the isotropic bulk behavior for large film thicknesses (i.e.,  $L_z > 4\bar{R}_G$ ). These results parallel those obtained from less coarse-grained simulation models (Refs. 15,19 and references therein).

(2) Chains close to the interface in a strongly segregated polymer mixture behave similarly. In order to reduce unfavorable interactions the largest axis of the ellipsoids orients parallel to the interface and shrinks in size so as to increase the number of favorable self-contacts inside the chain. These results qualitatively agree with those obtained in a detailed Monte Carlo study of the phase behavior of polymer blends by the bond-fluctuation model.<sup>25</sup>

(3) If a binary mixture of ellipsoids between two neutral walls undergoes spinodal decomposition, a lateral demixing length  $\lambda_{\parallel,m}$  is found, which increases for films thinner than the bulk demixing length ( $L_z < \lambda_m$ ). These results are in agreement with time-dependent Ginzburg–Landau theory.<sup>27</sup> Experimental studies of this effect have, to the best of our knowledge, not been performed yet. However, both the present simulations and theory lead to similar results and suggest that such studies should be promising.

(4) In the case where one of the two walls is structured, two different equilibrium patterns are found. Either the structure propagates through the whole film, leading to



a striped demixing pattern, or the surface-induced structure is confined to the vicinity of the wall. Both types of pattern are separated by a straight line in the  $L_z$ - $L_{\parallel}$  space, as can be explained by a consideration of surface energies only. Different equilibrium patterns lead to different kinetic pathways for the spinodal decomposition in such a film. In the case of an equilibrium pattern with full structure, pattern directed spinodal decomposition is the dominant process. The periodic ordered pattern freezes after reaching the opposite wall. On the other hand, the penetration depth of the pattern directed spinodal wave remains finite and lateral domain coarsening takes place in the late stages of decomposition. In the case of small pattern periodicity ( $L_{\parallel} < \lambda_m$ ), pattern directed spinodal decomposition is less pronounced, as the pattern induces unfavorable structures with too large interfaces.

In summary, the presented results suggest that the GEM is a promising model to study large length and time scales not only in the bulk, but also in the presence of interfaces. To test the model further we envisage to analyze the dependence of the structure of a thin polymer film on chain length. Several simulations<sup>39,40</sup> have already been devoted to this problem, with which we can compare our results. Furthermore, recent experiments<sup>41,42</sup> investigated the dependence of the radius of gyration on film thickness and obtained diverging results. We hope to contribute to this current discussion by the simulations envisaged.

## ACKNOWLEDGMENTS

We should like to thank W. Dieterich, B. Dünweg, R. Everaers and K. Kremer for interesting and stimulating discussions. Financial support by the Deutsche Forschungsgemeinschaft and the Ministère de l'Éducation Nationale, de la Recherche et de la Technologie in the framework of the European Graduate College "Soft Condensed Matter" (Konstanz-Strasbourg-Grenoble) is gratefully acknowledged.

## APPENDIX A: CALCULATION OF ELLIPSOID-WALL INTERACTION

The integrals in eq. (5) with a potential of the form eq. (6) and monomer densities, that are essentially sums and products of Gaussian functions, cf. eqs. (25a-c) in Ref. 10, can be cast into the more general form already treated in the appendix of Ref. 10. The six resulting integrals of eq. (5) are of the form

$$\int_{-\infty}^{+\infty} d^3y \chi(\mathbf{y}) \psi(y_3), \quad (\text{A1})$$

where the functions  $\chi(\mathbf{y})$  and  $\psi(y_3)$  are

$$\begin{aligned} \chi(\mathbf{y}) &= \frac{1}{(2\pi)^{3/2} \prod_{\alpha=1}^3 \sigma_{\alpha}} \exp\left(-\frac{1}{2} \sum_{\alpha} \left(\frac{x_{\alpha}(\mathbf{y})}{\sigma_{\alpha}}\right)^2\right), \\ x_{\alpha}(\mathbf{y}) &= \sum_{\beta} \mathcal{R}_{\alpha\beta}(y_{\beta} - w_{\beta}), \quad \sigma_{\alpha} = R_{\alpha} \sigma_{\alpha} \quad \text{and} \\ \psi(y_3) &= \exp\left(\pm \frac{y_3}{2l_w}\right). \end{aligned} \quad (\text{A2})$$

We adopted the notation and definitions of Ref. 10. An analogous calculation yields the same result for the integrals as in eqs. (C12-C14) of Ref. 10, except for the values of  $\mathcal{A}_{\alpha\beta}$ ,  $\mathcal{B}_{\alpha}$  and  $C$ , that in the present case read

$$\mathcal{A}_{\alpha\beta} = \mathcal{L}_{\alpha\beta}, \quad (\text{A3})$$

$$B_{\alpha} = \mp \frac{\delta_{\alpha 3}}{l_w} - 2 \sum_{\beta} \mathcal{L}_{\beta\alpha} w_{\beta}, \quad (\text{A4})$$

$$C = \sum_{\alpha,\beta} \mathcal{L}_{\alpha\beta} w_{\alpha} w_{\beta}. \quad (\text{A5})$$

The negative sign in front of the Kronecker-delta in eq. (A4) corresponds to the positive sign in eq. (A2) and vice versa.

In the case of a patterned substrate, we define  $l_{\parallel} = L_{\parallel}/4\pi$  and write for the first part of the wall potential

$$V(y_3) = \hat{\epsilon}_w \exp\left(-\frac{y_3}{2l_w}\right) \left[1 \pm \delta_w \cosh\left(\frac{iy_2}{2l_w}\right)\right]. \quad (\text{A6})$$

Thus the integration of the respective exponential functions can be performed as above. Only the form of  $B_{\alpha}$  changes, which now reads

$$B_{\alpha} = \frac{\delta_{\alpha 3}}{l_w} \mp \frac{\delta_{\alpha 2} i}{l_{\parallel}} - 2 \sum_{\beta} \mathcal{L}_{\beta\alpha} w_{\beta}, \quad (\text{A7})$$

where the negative sign refers to the first imaginary exponential function in eq. (A6), while the positive sign refers to the second one, respectively.

We note, that in our implementation the interaction between the walls and the ellipsoids is never cut off, in contrast to the interactions between the ellipsoids.<sup>10</sup>

## APPENDIX B: CALCULATION OF THE LATERAL FOURIER TRANSFORM OF THE DENSITY

The calculation of

$$\rho_{\parallel}(\mathbf{k}_{\parallel}, y_3) = \frac{1}{M(N+1)} \sum_{i=1}^M \int_{-\infty}^{+\infty} d^2y_{\parallel} e^{-i\mathbf{k}_{\parallel} \cdot \mathbf{y}_{\parallel}} \rho'_i(\mathbf{y}_{\parallel}, y_3) \quad (\text{B1})$$

is analogous to the derivation of  $\rho(\mathbf{k})$  given in appendix D of Ref. 10. Therefore we only present the result,

$$\begin{aligned} \rho_{\parallel}(\mathbf{k}_{\parallel}, y_3) &= \frac{1}{\sqrt{2\pi}} \frac{1}{(2+c_1)\sigma_1\sigma_2\sigma_3} \frac{1}{M} \sum_{i=1}^M \frac{1}{\sqrt{S_1^{(i)}S_2^{(i)}S_3^{(i)}}} \\ &\frac{1}{\sqrt{\det \mathcal{G}^{(i)}}} \frac{1}{\sqrt{2\mathcal{G}_{33}^{(i)-1}}} \exp\left(-\frac{1}{2} \sum_{\alpha=1}^2 \sum_{\beta=1}^2 k_{\alpha} \mathcal{G}_{\alpha\beta}^{(i)-1} k_{\beta}\right) \times \\ &\exp\left[\frac{1}{2} \left(\frac{i(y_3 - r_3^{(i)})}{\sqrt{2\mathcal{G}_{33}^{(i)-1}}} - \frac{1}{2\sqrt{2\mathcal{G}_{33}^{(i)-1}}} \sum_{\beta=1}^2 k_{\beta} \mathcal{G}_{3\beta}^{(i)}\right)^2\right] \times \\ &\exp\left(-i \sum_{\beta=1}^2 k_{\beta} r_{\beta}^{(i)}\right) \times \left\{ \exp\left(-\frac{1}{2} \frac{(\mathcal{R}_{13}^{(i)} \bar{u}_1)^2 S_1^{(i)}}{2\mathcal{G}_{33}^{(i)-1}}\right) \times \right. \\ &2 \cos\left[\frac{\mathcal{R}_{13} \bar{u}_1 \sqrt{S_1^{(i)}}}{2\mathcal{G}_{33}^{(i)-1}} \left(i(y_3 - r_3^{(i)}) - \frac{1}{2} \sum_{\beta=1}^2 k_{\beta} \mathcal{G}_{3\beta}^{(i)}\right) \right. \\ &\left. \left. + \sum_{\alpha=1}^2 k_{\alpha} \mathcal{R}_{1\alpha} \bar{u}_1 \sqrt{S_1^{(i)}}\right] + c_1 \right\}, \quad (\text{B2}) \end{aligned}$$

with

$$\mathcal{G}_{\alpha\beta}^{(i)} \equiv \sum_{\gamma} g_{\gamma}^{(i)} \mathcal{R}_{\gamma\alpha}^{(i)} \mathcal{R}_{\gamma\beta}^{(i)} \quad (\text{B3})$$

$$\mathcal{G}_{3\beta}^{(i)} \equiv \mathcal{G}_{\beta 3}^{(i)-1} + \mathcal{G}_{3\beta}^{(i)-1} \quad \text{and} \quad (\text{B4})$$

$$g_{\gamma}^{(i)} \equiv \left( (\sigma_1^2 S_1^{(i)})^{-1}, (\sigma_2^2 S_2^{(i)})^{-1}, (\sigma_3^2 S_3^{(i)})^{-1} \right). \quad (\text{B5})$$

The quantities  $\mathcal{R}_{\alpha\beta}^{(i)}$  and  $r_{\alpha}^{(i)}$  denote the rotation matrix and the center of mass of the  $i$ 'th particle respectively. The constants  $\sigma_1, \sigma_2, \sigma_3, c_1$  and  $\bar{u}_1$  are given in Tab. V of Ref. 10. Using eqs. (B2-B5) it is straightforward to calculate the lateral intermediate scattering function, eq. (13).

<sup>1</sup> K. Binder, Adv. Poly. Sci. **138**, 1 (1999).

<sup>2</sup> M. Böltau, S. Walheim, J. Mlynek, G. Krausch, and U. Steiner, Nature **391**, 877 (1998).

<sup>3</sup> E. Schäffer, T. Thurn-Albrecht, T. P. Russel, and U. Steiner, Nature **403**, 874 (2000).

<sup>4</sup> Z. Lin, T. Kerle, S. M. Baker, D. A. Hoagland, E. Schäffer, U. Steiner, and T. P. Russell, J. Chem. Phys. **114**, 2377 (2001).

<sup>5</sup> E. Schäffer, T. Thurn-Albrecht, T. P. Russel, and U. Steiner, Europhys. Lett. **53**, 518 (2001).

<sup>6</sup> E. Reister, M. Müller, and K. Binder, Phys. Rev. E **64**, 041804 (2001).

<sup>7</sup> M. Murat and K. Kremer, J. Chem. Phys. **108**, 4340 (1998).

<sup>8</sup> P. G. Bolhuis, A. A. Louis, J. P. Hansen, and E. J. Meijer, J. Chem. Phys. **114**, 4296 (2001).

<sup>9</sup> P. G. Bolhuis, A. A. Louis, and J. P. Hansen, Phys. Rev. E **64**, 021801 (2001).

<sup>10</sup> F. Eurich and P. Maass, J. Chem. Phys. **114**, 7655 (2001).

<sup>11</sup> The system coordinates are denoted by  $\mathbf{y} = (y_1, y_2, y_3) \equiv (x, y, z)$ . The  $x$ - and  $y$ -direction are parallel, the  $z$ -direction is perpendicular to the walls.

<sup>12</sup> J. Israelachvili, *Intermolecular and Surface Forces* (Academic Press, San Diego, 2000).

<sup>13</sup> G. S. Grest and M. Murat "Computer Simulations of Tethered Chains" in "Monte Carlo and Molecular Dynamics Simulations in Polymer Science" by K. Binder (ed.), Oxford University Press (1995), and references therein.

<sup>14</sup> D. Y. Yoon, M. Vacatello, and G. D. Smith "Simulation Studies of Polymer Melts at Interfaces" in "Monte Carlo and Molecular Dynamics Simulations in Polymer Science" by K. Binder (ed.), Oxford University Press (1995), and references therein.

<sup>15</sup> C. Mischler, J. Baschnagel, and K. Binder, Adv. Coll. Interf. Sci. **94**, 197 (2001).

<sup>16</sup> A. Yethiraj, J. Chem. Phys. **101**, 2489 (1994).

<sup>17</sup> A. Yethiraj and C. K. Hall, Macromolecules **23**, 1865 (1990).

<sup>18</sup> We used the symmetry with respect to  $L_z/2$  in the representation of the data. The non-continuous drop to zero at  $z \approx 0$  is an artefact of the analysis, because the center of mass density goes to zero in this region, cf. Fig. 1.

<sup>19</sup> J. Baschnagel, K. Binder, and A. Milchev, "Mobility of Polymers Near Surfaces" in "Polymer Surfaces, Interfaces and Thin Films" by A. Karim and S. Kumar (eds.), World Scientific, Singapore (2000).

<sup>20</sup> R. S. Pai-Panandiker, J. R. Dorgan, and T. Pakula, Macromolecules **30**, 6348 (1997).

<sup>21</sup> J. H. van Vliet and G. ten Brinke, J. Chem. Phys. **93**, 1436 (1990).

<sup>22</sup> H. Tang, I. Szleifer, and S. K. Kumar, J. Chem. Phys. **100**, 5367 (1993).

<sup>23</sup> Y. Rouault, J. Baschnagel, and K. Binder, J. Stat. Phys. **80**, 1009 (1995).

<sup>24</sup> D. P. Landau and K. Binder *A Guide to Monte Carlo Simulations in Statistical Physics* (Cambridge University Press, Cambridge, 2000).

<sup>25</sup> M. Müller, K. Binder, and W. Oed, J. Chem. Soc. Faraday Trans. **91**, 2369 (1995).

<sup>26</sup> M. Müller, Macromolecules **31**, 9044 (1998).

<sup>27</sup> H. P. Fischer, P. Maass, and W. Dieterich, Europhys. Lett. **42**, 49 (1998).

<sup>28</sup> R. Kenzler, F. Eurich, P. Maass, B. Rinn, J. Schropp, E. Bohl, and W. Dieterich, Comp. Phys. Comm. **133**, 139 (2001).

<sup>29</sup> S. Puri and H. L. Frisch, J. Phys.: Condens. Matter **9**, 2109 (1997).

<sup>30</sup> G. Krausch, C. Dai, J. Kramer, and J. F. Marko, Macromolecules **26**, 5566 (1993).

<sup>31</sup> K. Fukunaga, H. Elbs, and G. Krausch, Langmuir **16**, 3474 (2000).

<sup>32</sup> P. Lenz and R. Lipowski, Phys. Rev. Lett. **80**, 1920 (1998).

- <sup>33</sup> A. Karim, J. F. Douglas, B. P. Lee, S. C. Glotzer, J. A. Rogers, R. J. Jackman, E. J. Amis, and G. M. Whitesides, *Phys. Rev. E* **57**, R6273 (1998).
- <sup>34</sup> L. Kielhorn and M. Muthukumar, *J. Chem. Phys.* **111**, 2259 (1999).
- <sup>35</sup> Strictly speaking,  $\lambda_{\parallel,m}$  is the relevant length scale for lateral decomposition in a slab. However, for  $L_z = 12.5$  the demixing length  $\lambda_{\parallel,m}$  is close to the bulk value  $\lambda_m$ , cf. Sec. IV C.
- <sup>36</sup> K. Šolc and W. H. Stockmayer, *J. Chem. Phys.* **54**, 2756 (1971); *J. Chem. Phys.* **55**, 335 (1971).
- <sup>37</sup> J. A. Aronovitz and D. R. Nelson, *J. Physique* **47**, 1445 (1986).
- <sup>38</sup> H. W. H. M. Janszen, T. A. Tervoort, and P. Cifra, *Macromolecules* **29**, 5678 (1996).
- <sup>39</sup> J.-S. Wang and K. Binder, *J. Phys. I France* **1**, 1583 (1991).
- <sup>40</sup> I. A. Bitsanis and G. Hadziioannou, *J. Chem. Phys.* **92**, 3827 (1990).
- <sup>41</sup> J. Kraus, P. Müller-Buschbaum, T. Kuhlmann, D. W. Schubert, and M. Stamm, *Europhys. Lett.* **49**, 210 (2000).
- <sup>42</sup> R. L. Jones, S. K. Kumar, D. L. Ho, R. M. Briber, and T. P. Russell, *Macromolecules* **34**, 559 (2001).

TABLE I. System sizes for homogeneous films.

$L_z$	25	17	12.5	10	8
$L_x, L_y$	69.28	84.02	97.98	109.54	122.47
$L_z$	6	4	3	2	1.5
$L_x, L_y$	141.42	173.21	200.00	244.95	282.84

TABLE II. System sizes for films of binary mixtures.

$L_z$	50	25	12.5	6	4	3	2
$L_x, L_y$	69.28	97.98	138.56	200.00	244.95	282.84	346.41

TABLE III. System sizes for films of binary mixtures on structured surfaces.

$L_{\parallel} = 50:$						
$L_z$	50	25	12.5	6	4	
$L_y$	–	100	150	200	250	
$L_x$	–	96.26	128.34	200.53	240.64	
$L_{\parallel} = 25:$						
$L_z$	50	25	12.5	6	4	
$L_y$	75	100	150	200	250	
$L_x$	64.17	96.26	128.34	200.53	240.64	
$L_{\parallel} = 12.5:$						
$L_z$	50	25	12.5	6	4	
$L_y$	75	100	137.5	200	250	
$L_x$	64.17	96.26	140.01	200.53	240.64	
$L_{\parallel} = 6:$						
$L_z$	50	25	12.5	6	4	
$L_y$	72	102	138	204	246	
$L_x$	66.84	94.37	139.50	196.60	244.55	

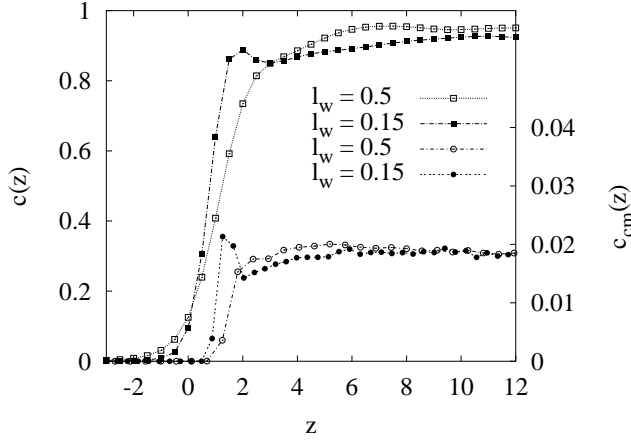


FIG. 1. Monomer density  $c(z)$  (upper curves) and center of mass density  $c_{\text{cm}}(z)$  (lower curves) for wall potentials with  $l_w = 0.5$  (open symbols) and  $l_w = 0.15$  (full symbols). The film width is  $L_z = 25$ .

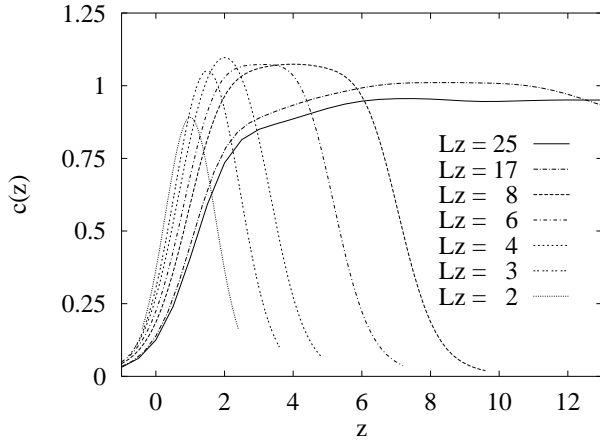


FIG. 2. Monomer density as a function of distance  $z$  from the wall for  $l_w = 0.5$  for various film thicknesses  $L_z$ .

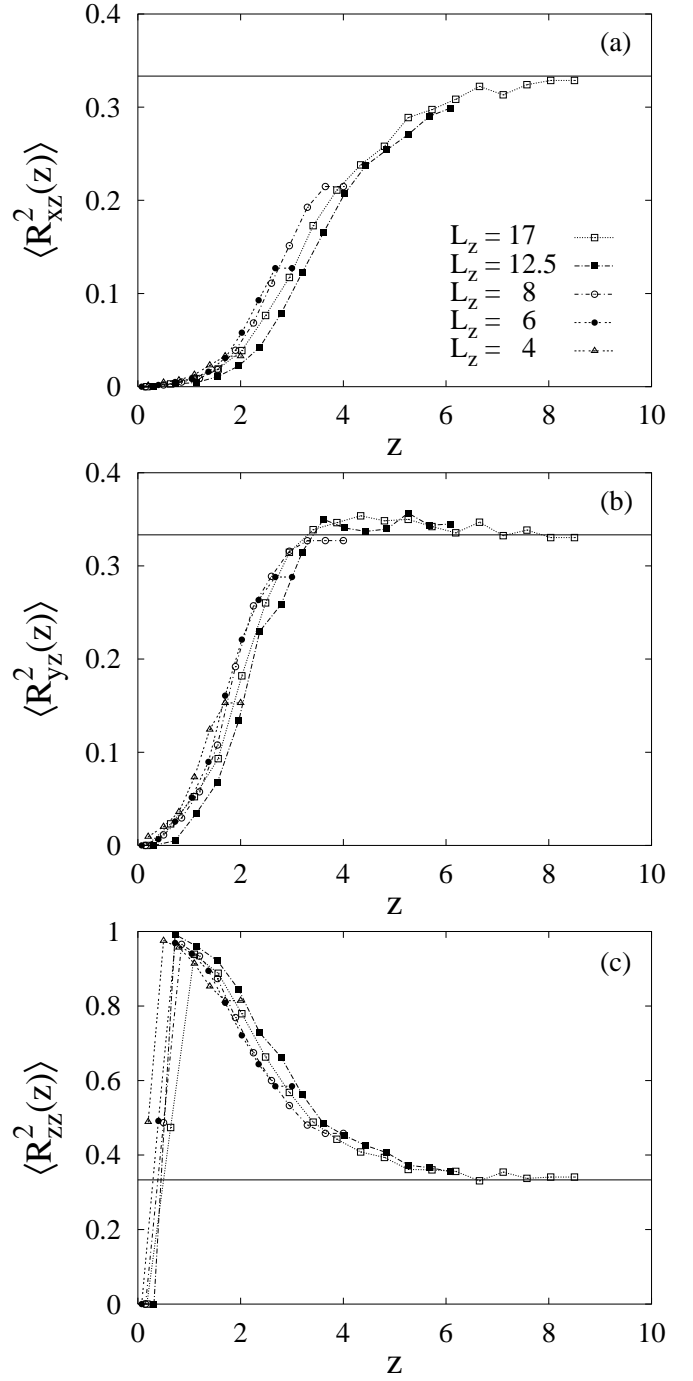


FIG. 3. Lateral averaged squared matrix elements  $\langle R_{\alpha\beta}^2(z) \rangle$  are shown characterizing the orientation of the ellipsoids with respect to the  $z$ -axis of the system. The alignment of the principal axis corresponding to the largest eigenvalue is given in (a), to the second eigenvalue in (b), and to the smallest one in (c). The expected value  $1/3$  for totally random oriented ellipsoids is marked in as a straight line each time. The results are shown for different film widths  $L_z$  and  $l_w = 0.5$ .

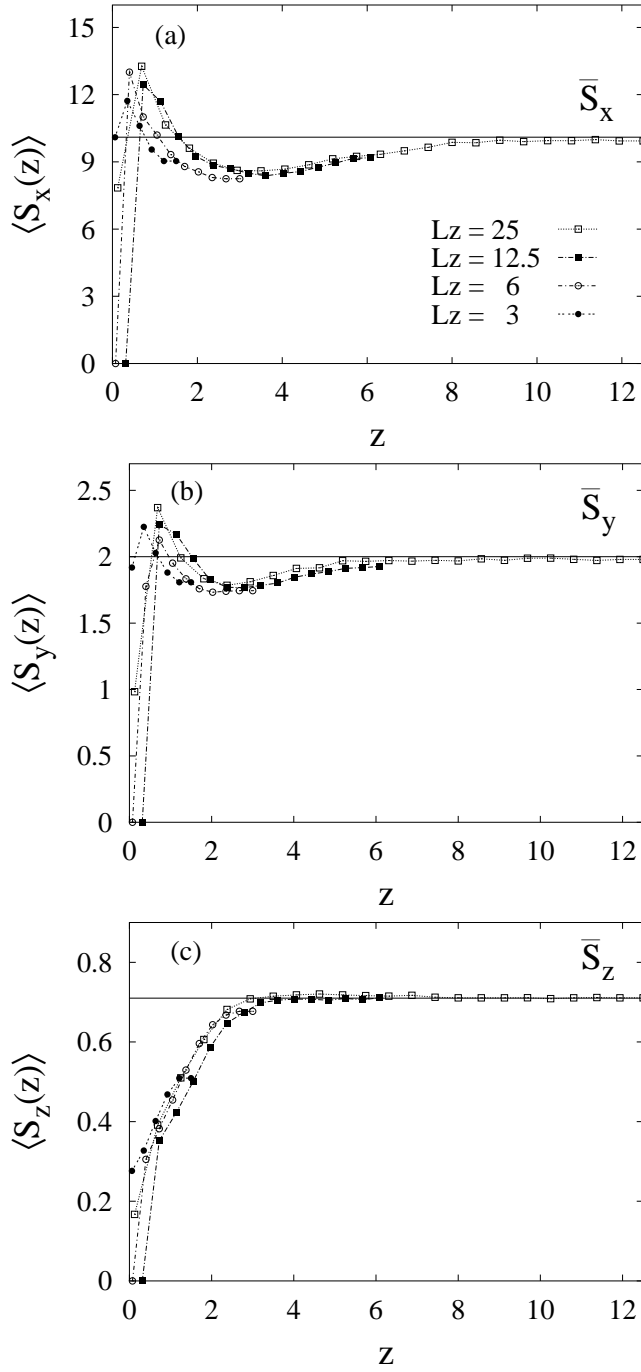


FIG. 4. Lateral averaged eigenvalues  $\langle S_\alpha(z) \rangle$  as a function of the separation  $z$  from the wall. The expected bulk values from simulations with periodic boundary conditions<sup>10</sup> are shown additionally. The results are given for different film widths  $L_z$  and  $l_w = 0.5$ .

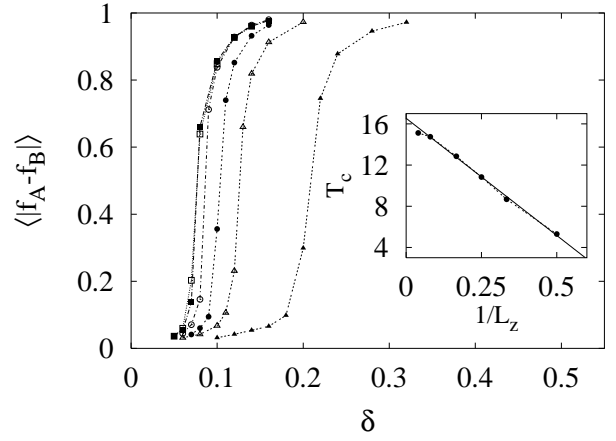


FIG. 5. Coexistence curves for different film thicknesses  $L_z = 25(\square), 12.5(\blacksquare), 6(\circ), 4(\bullet), 3(\triangle), 2(\blacktriangle)$ . The extrapolated critical temperatures as a function of  $1/L_z$  are given in the inset.

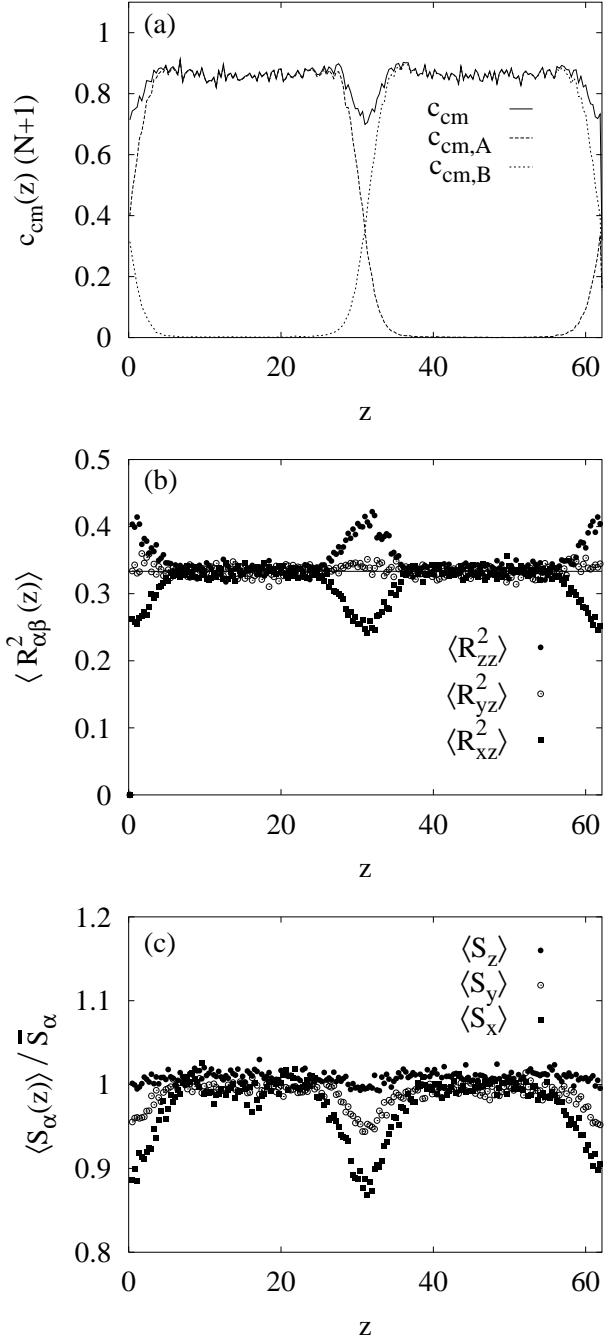


FIG. 6. Normalized center of mass density (a), squared rotational matrix elements (b) and eigenvalues (c) as a function of distance  $z$  from the interfaces for a separated  $A$ - $B$  mixture.

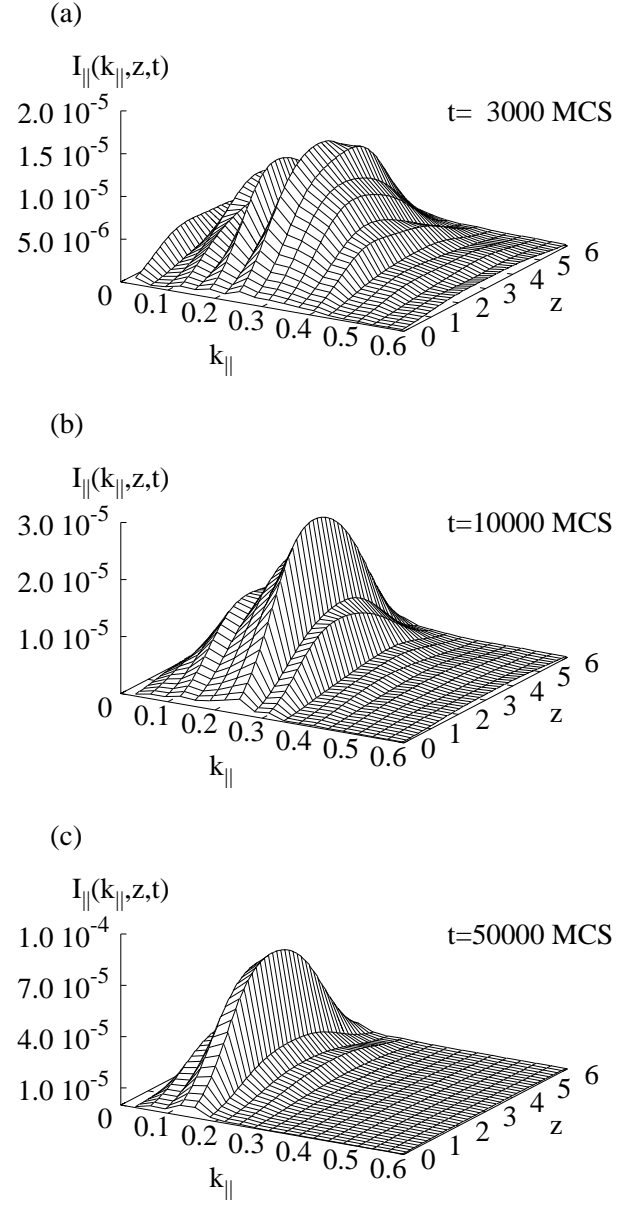


FIG. 7. Lateral intermediate scattering function  $I_{\parallel}(k_{\parallel}, z, t)$  for a film of thickness  $L_z = 6$  shown at various times (a)  $t = 3000$  MCS, (b)  $t = 10000$  MCS and (c)  $t = 50000$  MCS.

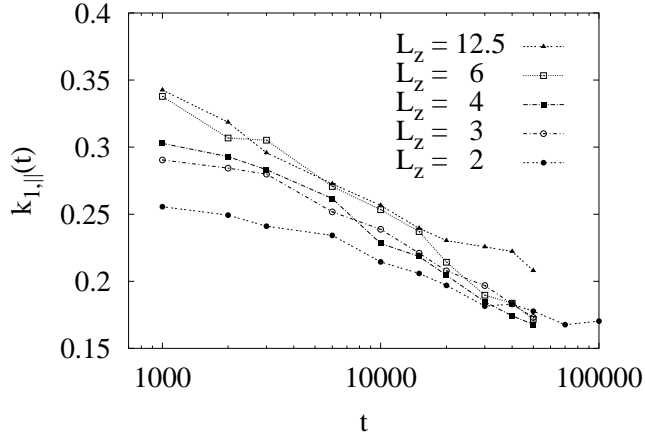


FIG. 8. Film averaged first moment of the lateral intermediate scattering function  $k_{1,||}(t)$ , eq. (14), as a function of time for different film thicknesses  $L_z$ .

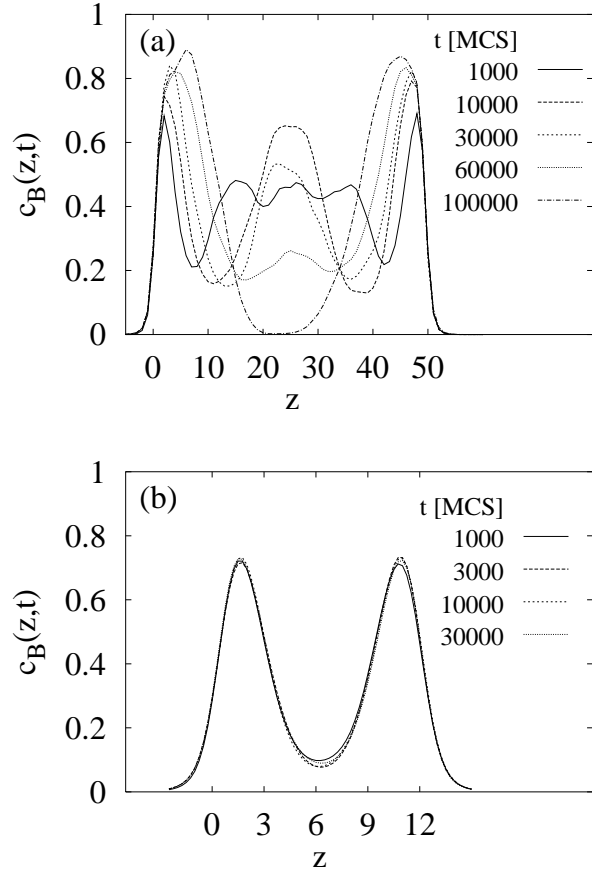


FIG. 9. Laterally averaged monomer concentration  $c_B(z)$  of the  $B$ -ellipsoids, for different times, in a film of thickness (a)  $L_z = 50$  and (b)  $L_z = 12.5$ . The mismatch wall interaction is  $\delta_w = 0.5$  for both walls.

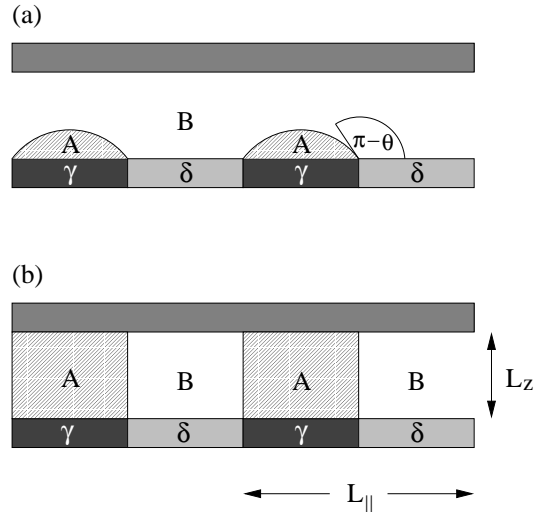


FIG. 10. Two possible structures on a patterned substrate. Upper figure (a): The polymer film is only patterned near the surface (“partial structure”). Lower figure (b): The polymer structure induced by the surface penetrates the film (“full structure”).

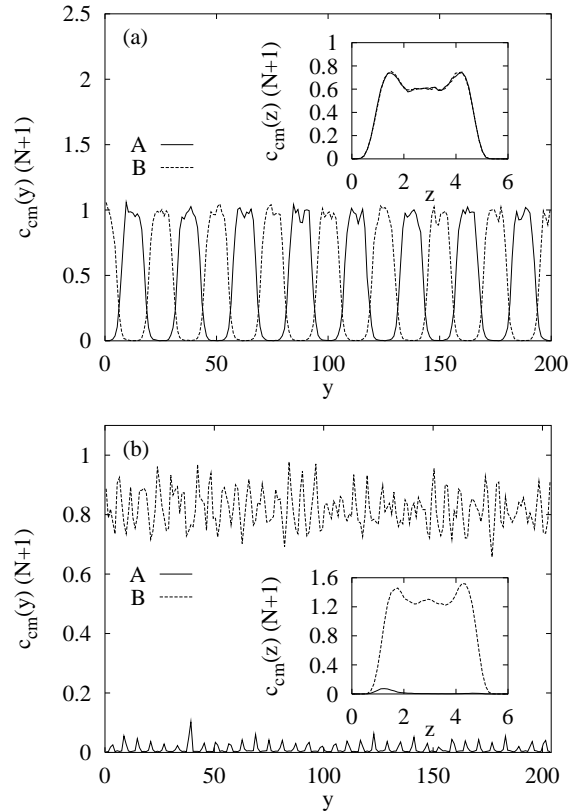


FIG. 11. Results for the normalized center of mass density  $c_{cm}$  as a function of  $y$  and  $z$  (shown in the respective inset) in the case of (a) full, and (b) partial structure. The film thickness is  $L_z = 6$  in both cases and the periodicity of the structure is (a)  $L_{||} = 25$  and (b)  $L_{||} = 6$ .



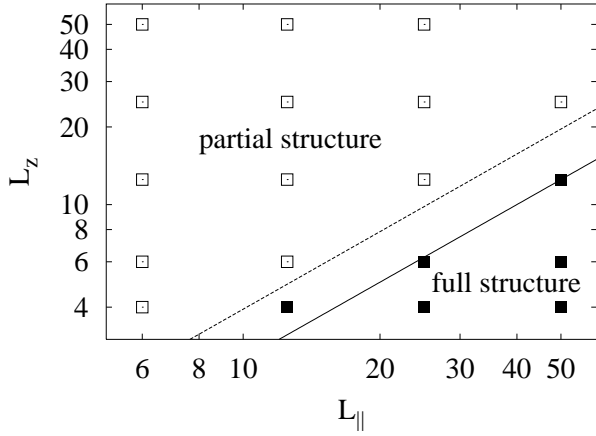


FIG. 12. Regions in the  $L_z$ - $L_{\parallel}$  plane, where the domain pattern in the slab is fully structured (■) and only partially structured (□), in double logarithmic representation. The dividing lines are given by the two limiting cases of eq. (18),  $L_z = 1/4 L_{\parallel}$  (straight line) and  $L_z = \pi/8 L_{\parallel}$  (dashed line).

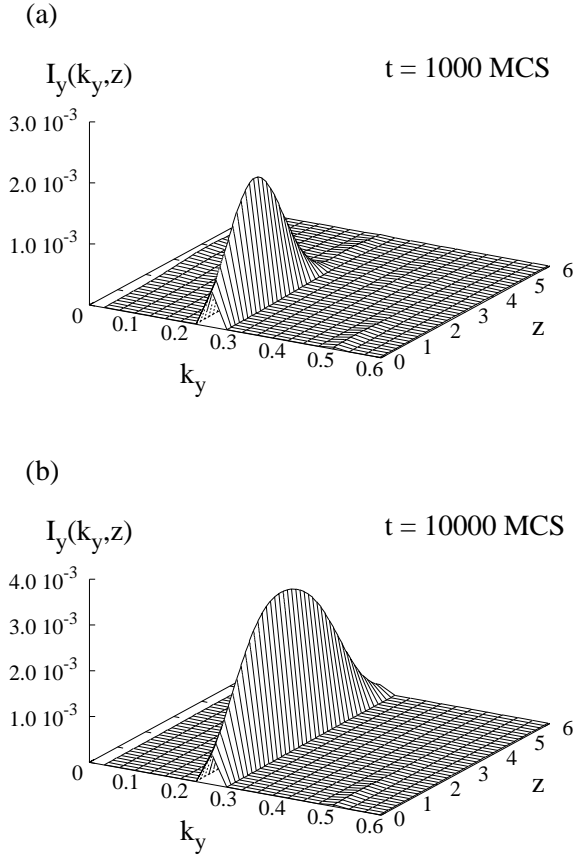


FIG. 13. Intermediate scattering function  $I_y(k_y, z, t)$  for a system of  $L_{\parallel} = 25$  and  $L_z = 6$  at times (a)  $t = 1000$  MCS and (b)  $t = 10000$  MCS. The patterned structure is stable throughout the whole film.

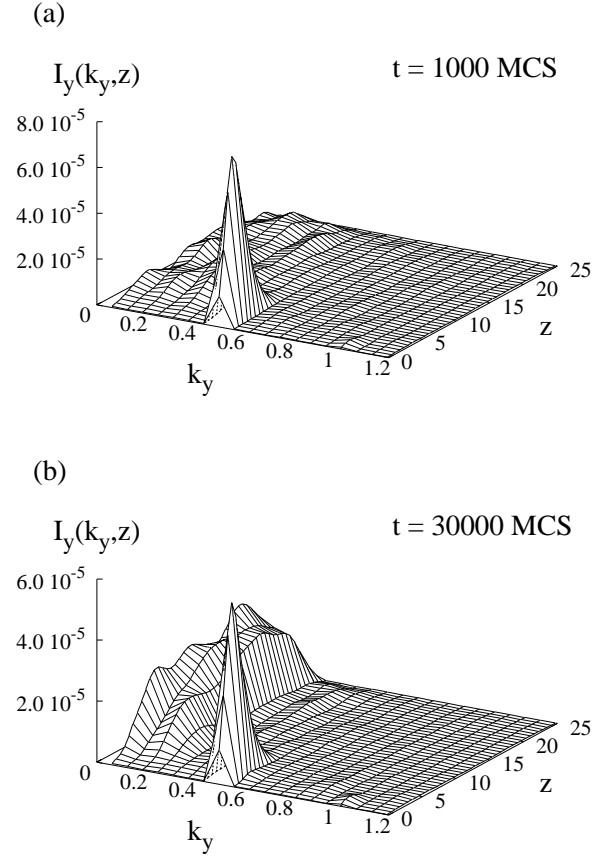
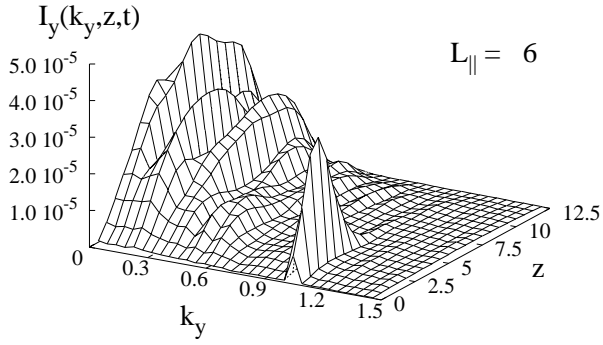
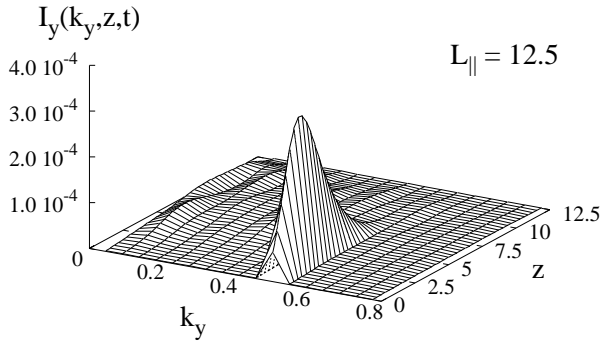


FIG. 14. Intermediate scattering function  $I_y(k_y, z, t)$  for a system of  $L_{\parallel} = 12.5$  and  $L_z = 25$  at times (a)  $t = 1000$  MCS and (b)  $t = 30000$  MCS. Lateral domain coarsening occurs away from the vicinity of the patterned wall. Near the wall the structure changes only weakly.

(a)



(b)



(c)

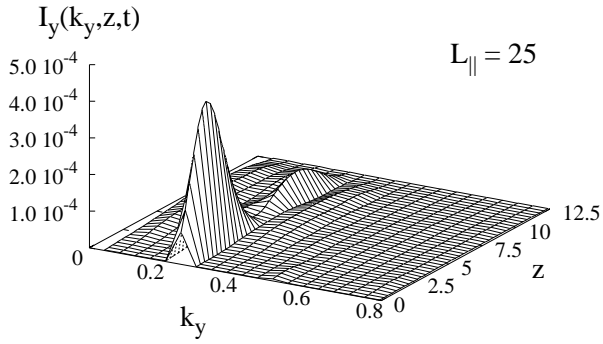


FIG. 15. Intermediate scattering function  $I_y(k_y, z, t)$  for early demixing times  $t = 1000$  MCS and film thickness  $L_z = 12.5$ . The pattern periodicity is (a)  $L_{\parallel} = 6$ , (b)  $L_{\parallel} = 12.5$  and (c)  $L_{\parallel} = 25$ .

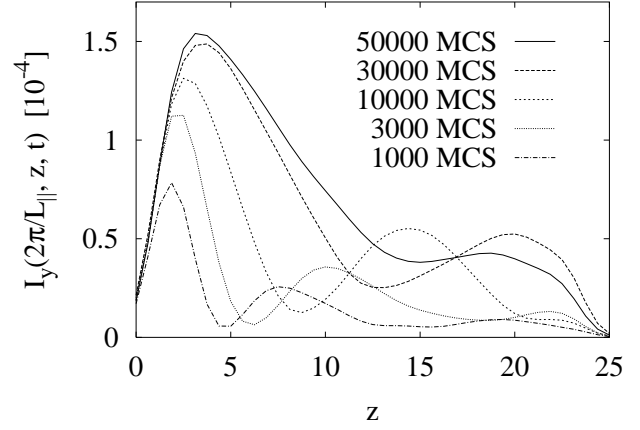


FIG. 16. Intermediate scattering function  $I_y(2\pi/L_{\parallel}, z, t)$  as a function of time. The film thickness is  $L_z = 25$  and the pattern periodicity  $L_{\parallel} = 50$ .